chemosensors

MDPI

Article

Phosphorescent O_2-Probes Based on Ir(III) Complexes for Bioimaging Applications

Mozhgan Samandarsangari [1], Ilya S. Kritchenkov [1], Daria O. Kozina [1], Anastasia D. Komarova [2,3], Marina V. Shirmanova [2] and Sergey P. Tunik [1,*]

[1] Institute of Chemistry, St. Petersburg State University, Universitetskaya Embankment 7-9, 199034 St. Petersburg, Russia
[2] Institute of Experimental Oncology and Biomedical Technologies, Privolzhskiy Research Medical University, Minin and Pozharsky sq. 10/1, 603005 Nizhny Novgorod, Russia
[3] Institute of Biology and Biomedicine, Lobachevsky State University of Nizhny Novgorod, Gagarina av., 23, 603950 Nizhny Novgorod, Russia
* Correspondence: s.tunik@spbu.ru

Abstract: The design, synthesis, and investigation of new molecular oxygen probes for bioimaging, based on phosphorescent transition metal complexes are among the topical problems of modern chemistry and advanced bioimaging. Three new iridium $[Ir(N^C)_2(N^N)]^+$ complexes with cyclometallating 4-(pyridin-2-yl)-benzoic acid derivatives and different di-imine chelate ligands have been synthesized and characterized by mass spectrometry and NMR spectroscopy. The periphery of these complexes is decorated with three relatively small "double-tail" oligo(ethylene glycol) fragments. All these complexes exhibit phosphorescence; their photophysical properties have been thoroughly studied, and quantum chemical calculations of their photophysical properties were also performed. It turned out that the changes in the nature of the di-imine ligand greatly affected the character of the electronic transitions responsible for their emission. Two complexes in this series show the desired photophysical characteristics; they demonstrate appreciable quantum yield (14–15% in degassed aqueous solutions) and a strong response to the changes in oxygen concentration, ca. three-fold increase in emission intensity, and an excited state lifetime upon deaeration of the aqueous solution. The study of their photophysical properties in model biological systems (buffer solutions containing fetal bovine serum—FBS) and cytotoxicity assays (MTT) showed that these complexes satisfy the requirements for application in bioimaging experiments. It was found that these molecular probes are internalized into cultured cancer cells and localized mainly in mitochondria and lysosomes. Phosphorescent lifetime imaging (PLIM) experiments showed that under hypoxic conditions in cells, a 1.5-fold increase in the excitation state lifetime was observed compared to aerated cells, suggesting the applicability of these complexes for the analysis of hypoxia in biological objects.

Keywords: oxygen sensing; iridium complexes; phosphorescence; hypoxia; bioimaging; phosphorescence lifetime imaging

Citation: Samandarsangari, M.; Kritchenkov, I.S.; Kozina, D.O.; Komarova, A.D.; Shirmanova, M.V.; Tunik, S.P. Phosphorescent O_2-Probes Based on Ir(III) Complexes for Bioimaging Applications. *Chemosensors* **2023**, *11*, 263. https://doi.org/10.3390/chemosensors11050263

Academic Editors: Andrea Gaiardo, Barbara Fabbri and Vincenzo Guidi

Received: 21 February 2023
Revised: 12 April 2023
Accepted: 21 April 2023
Published: 28 April 2023

1. Introduction

Molecular oxygen is one of the key physiological components of aerobic organisms. Monitoring its concentration in biological objects makes possible evaluation of the object's metabolic status, the presence of pathological changes, or the efficacy of the therapy used to combat the pathology [1–4]. For these and a number of other reasons, which are discussed in a wide range of original papers and reviews [5–12], the development of molecular oxygen probes to be used in biomedical experiments is one of the most important areas of functional biomedical imaging.

Among a number of probes applicable for noninvasive determination of O_2 content, phosphorescent complexes of transition metals stand out in particular. The presence of a sensory response to molecular oxygen in phosphorescent metal complexes is related to

the triplet character of their emission and the ability of oxygen molecules to quench it, which results in a strong reduction in emission intensity and lifetime [5,13,14]. Measuring intensity/lifetime variations vs. oxygen concentration allows for building up the calibration curves, which make it possible to quantify the content of O_2 in the objects under study. The calibrations as well as the experimental determination of oxygen concentration can be conducted by two independent approaches based either on emission intensity (a ratiometric approach) or phosphorescence lifetime measurements. The latter is a time-resolved technique that is becoming more and more widespread in luminescent microscopy and is also called phosphorescence lifetime imaging (PLIM). In bioimaging experiments, the PLIM approach has a number of advantages; one of them is that there is no need to use internal or external oxygen-insensitive emission standards, whereas the other advantage consists in the independence of the sensory response from the variations in optical characteristics of studied samples that may disturb correlative readings of ratiometric probes. The time-resolved techniques, including PLIM, were successfully used for quantitative mapping of the oxygen distribution in various biological samples by using probes based on highly sensitive Pt and Pd porphyrins [5,11,12,15–17]. In these molecules, the chromophores have been shielded from side interactions (primarily with albumin, which actively forms adducts with hydrophobic molecules) either by packing into polymeric nanoparticles [18–29] or into a corona of high molecular weight poly(ethylene glycol) substituents at the porphyrin ligands [30–40]. These probes are commercially available, but they are not free from some significant drawbacks, such as their large size that prevents internalization through the cell membrane [30–40] or the instability of the nanospecies in physiological media [12,41].

However, recently, another type of molecular probe based on iridium complexes has been designed and used for oxygen distribution studies in living cell cultures [42–46]. Similar to the Pt and Pd porphyrins [30–40], these emitters are shielded from side interactions with the components of physiological media by oligo(ethylene glycol) (OEG) substituents in the ligand environment, which also increase the probes solubility in aqueous media and their biocompatibility, but the length of the OEG chains is substantially shorter compared to that used in the Pt and Pd porphyrine probes [30–40]. The OEG corona in the iridium complexes still protects the chromophores from side interactions, but the size of the probe does not exceed 1–2 nanometers, which allows probe internalization into cells and makes possible mapping of molecular oxygen distribution even in individual organelles and cell compartments. Alternative approaches to imparting the iridium-based probes biocompatibility and stabilizing their photophysical parameters are conjugation of the chromophores with albumin [47] or embedding them into polymeric micelles [48]. It is also worth noting that the photophysical characteristics of the probes, for example, emission/excitation wavelengths and excited state lifetimes, very often have to be fine-tuned to meet the requirements of certain experiments, which implies the development of a broad range of probes of different composition and structure. These requirements may stem from the properties of the biological sample under study or may be determined by the parameters of the instruments used in a particular bioimaging experiment.

In this article, we present the synthesis, characterization, and photophysical study of three novel phosphorescent $[Ir(N^{\wedge}C)_2(N^{\wedge}N)]^+$ complexes (**Ir1**–**Ir3**) containing identical metallated N^C and different di-imine N^N ligands, which were decorated with oligo(ethylene glycol) substituents to make these compounds water-soluble and biocompatible. The oxygen sensing properties of the most effective emitters (**Ir2** and **Ir3**) were also investigated in model physiological media and in living cells by using time-resolved PLIM mode.

2. Materials and Methods

Reagents: 4-(2-pyridyl)benzoic acid [49], 2-azidopyridine [50], 4-oxo-4-(prop-2-ynyloxy) butanoic acid [51], and 2,5,8,12,15,18-hexaoxanonadecan-10-amine [52] (NH_2-2OEG) were synthesized according to the literature methods. Modified synthetic procedures were used to obtain 4-Oxo-4-((1-(pyridin-2-yl)-1H-1,2,3-triazol-4-yl)methoxy)-butanoic acid [53] and its OEG-derivative N^N2 [44], as well as 4-(2-(pyridin-2-yl)-1H-phenanthro [9,10-

d]imidazol-1-yl)benzoic acid [45] and its OEG-derivative N^N3 [45]. Synthesis of the N^C ligand, $[Ir_2(N^C)_4Cl_2]$ dimer, and target complexes **Ir1**–**Ir3**, as well as modified synthetic protocols for 4-Oxo-4-((1-(pyridin-2-yl)-1H-1,2,3-triazol-4-yl)methoxy)-butanoic acid, (4-(2-(pyridin-2-yl)-1H-phenanthro [9,10-d]imidazol-1-yl)benzoic acid, N^N2 and N^N3 ligands, are described in the Supplementary Information File S1. Other solvents and reagents were received from Merck (Darmstadt, Germany) and Vekton (St. Petersburg, Russia) and used without additional purification.

The 1D ^{1}H, 2D COSY ^{1}H-^{1}H NMR spectra were measured using the Bruker Avance 400 MHz; the solvent residual signals were used to reference the chemical shift values. Mass spectra (ESI, positive mode) were recorded using an HRMS-ESI spectrometer (Bruker maXis QTOF).

Details of photochemical and computational experiments, as well as data concerning the description of installations and methods for conducting biological research, are given in the Supplementary Information File S1.

3. Results and Discussion

3.1. Synthesis and Characterization

As a platform for the synthesis of the probes, we chose iridium bis-cyclometallated complexes, $[Ir_2(N^C)_4(N^N)]^+$, in which a di-imine moiety is used as the third chelating ligand. Double-tailed oligo(ethylene glycol) fragments are attached to all ligands in the coordination sphere of these complexes to protect the chromophores from side interactions with the components of biological samples and to impart water solubility to the probes. For this purpose, the initial organic compounds (N^C pro-ligand) and the N^N di-imine chelates were appropriately modified by the introduction of OEG tails by using either the literature procedures (in the case of N^N2 and N^N3 ligands) or the approaches shown below (Scheme 1) in the case of the newly synthesized compounds (N^C pro-ligand and N^N1).

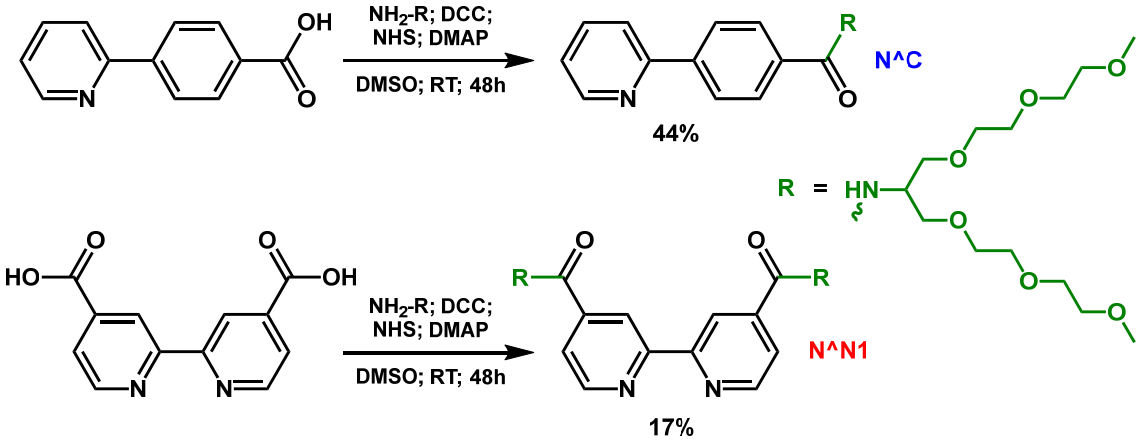

Scheme 1. Synthetic scheme of the new ligands N^C and N^N1.

The obtained cyclometallating ligand was employed in reaction with iridium chloride, which affords the dimeric Ir(III) complex $[Ir_2(N^C)_4Cl_2]$. The further interaction of the dimer with the corresponding di-imines gave the target complexes **Ir1**–**Ir3** (Scheme 2) a moderate yield (30–48%). For details of the synthetic protocols and characteristics of the obtained compounds, see the Supporting Information file.

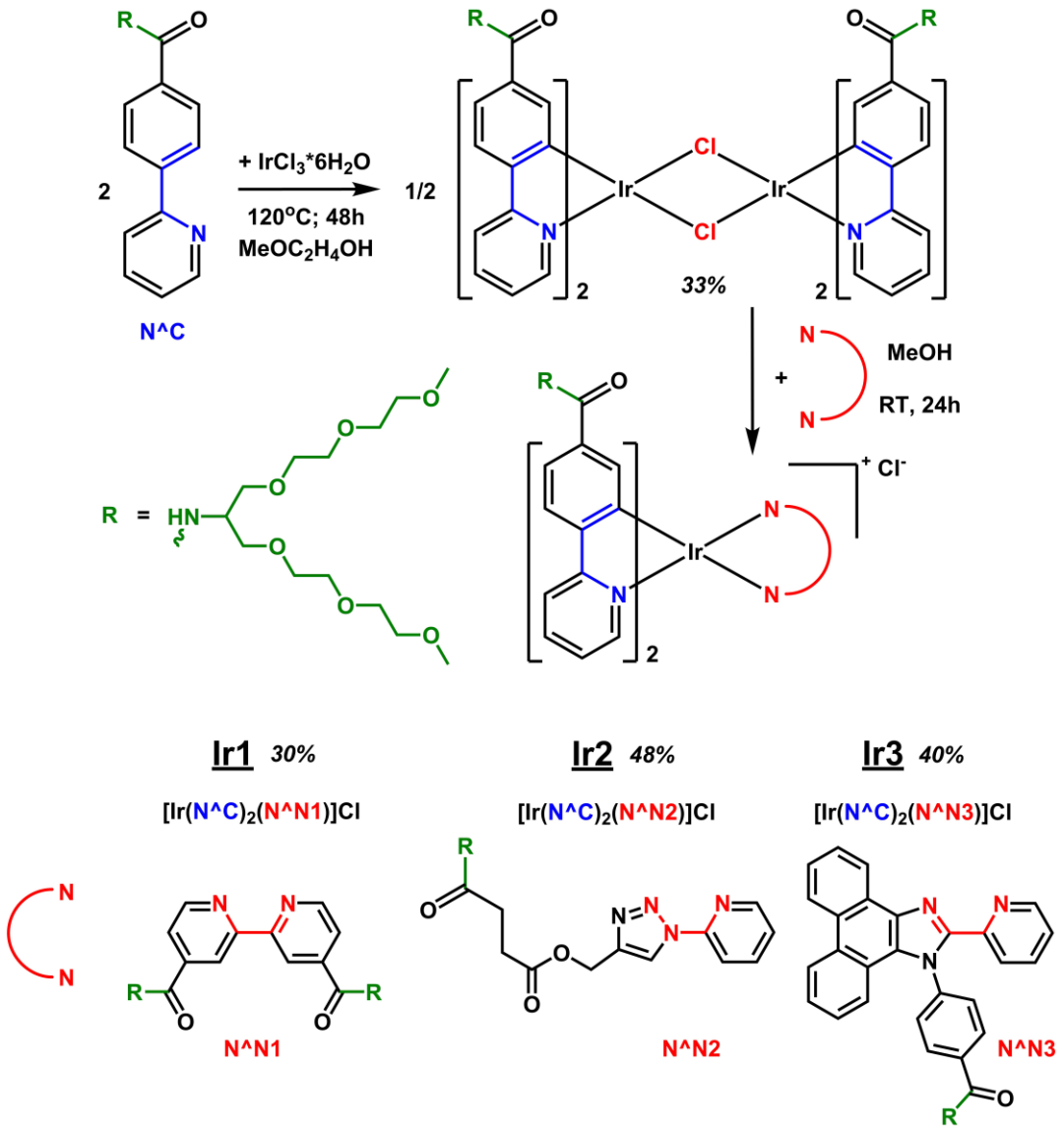

Scheme 2. Scheme of synthesis of new Ir(III) dimer $[Ir_2(N^C)_4Cl_2]$ and new complexes **Ir1**–**Ir3**.

The newly synthesized substances (a novel N^C ligand, a dimeric complex, and three target iridium compounds, **Ir1**–**Ir3**) are viscous, non-crystallizable compounds due to the presence of the OEG substituents in their structure. This property neither allows the crystallization and application of X-ray crystallography for the structural characterization of these molecules nor the performance of a qualitative elemental analysis. Nevertheless, all substances were studied with a set of modern physicochemical methods of analysis, including 1D ^{1}H, 2D ^{1}H-^{1}H COSY NMR spectroscopy, and high-resolution ESI mass spectrometry, which make it possible to reliably establish their composition and structure. A detailed description of the obtained NMR and mass spectra, as well as the assignment of the observed signals, is given in the Supplementary Information File S1 (Figures S1–S18).

We carried out quantum chemical calculations with the aim of optimizing the structures of complexes in the ground state and elucidating the nature of the electronic transitions responsible for the processes of excitation and emission. As an example, Figure 1 shows the **Ir1-0** complex, which differs from the obtained **Ir1** complex in the absence of OEG fragments in order to simplify calculations without substantial changes in the nature of the chromophoric center. The other optimized structures (**Ir2-0** and **Ir3-0** for complexes **Ir2** and **Ir3**, respectively) are shown in the Supplementary Materials File S1 (Figures S22 and S23). The optimized structural patterns obtained for iridium complexes display the architecture

typical for this type of iridium bis-cyclometallated complex. The nitrogen and carbon atoms of the N^C ligands are disposed in the trans- and cis-positions of the coordination octahedron, respectively, and the di-imine chelate completes the coordination environment of the Ir(III) ion. The key structural parameters of **Ir1-0**, **Ir2-0,** and **Ir3-0** optimized structures (see Tables S9–S11) are not exceptional and fit well with the characteristics of previously obtained iridium complexes of this type [54–56]. It is also worth noting that mass spectroscopic and ^{1}H NMR data (Figures S1–S18) are in complete agreement with the optimized structures. The major signals observed in ESI$^+$ mass spectra represent $[Ir(N^C)_2(N^N)]^+$ molecular ions (with or without addition of H^+ or Na^+ ions), thus confirming the molecular stoichiometry of the obtained compounds. In turn, the number of signals in the proton NMR spectra, their multiplicity, and their relative intensity fit well with the structural patterns shown in Figure 1, Figure S22, and Figure S23.

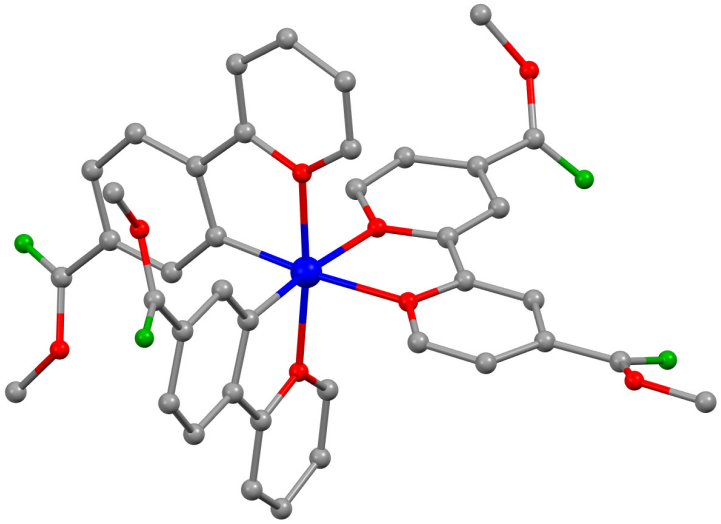

Figure 1. Optimized structure of the model **Ir1-0** complex (hydrogen atoms are omitted for clarity). The calculations have been simplified by substituting OEG pendants in **Ir1** complex with methyl groups in **Ir1-0** structure. Atom colors: Ir-blue; N-red; O-green; C-gray.

3.2. Photophysical Study

The **Ir1**–**Ir3** complexes exhibit luminescence in a rather wide range of wavelengths (with emission band maxima varying from 502 to 651 nm) and quantum yields up to 15% in deaerated water. The complexes display large Stokes shifts (from 90 to 165 nm), excited state lifetimes in the microsecond domain, and substantial dependence of luminescence intensity and lifetime on the presence of molecular oxygen, which is indicative of the triplet nature of their emissive excited states, i.e., phosphorescence. Absorption and emission spectra of **Ir1**–**Ir3** in aqueous solution are shown in Figure 2, and numerical spectroscopic data are summarized in Table 1.

Table 1. Photophysical data for complexes **Ir1**–**Ir3** in aqueous solutions at 310 K.

	λ_{abs} (nm)	λ_{em} (nm)	Φ_{aer} (%)	Φ_{deg} (%)	τ_{aer} (ns)	τ_{deaer} * (ns)	τ_{deg}/τ_{aer}
Ir1 [a]	256; 271sh; 290sh; 317sh; 348; 388sh; 421sh; 486sh	651	1.5	2.0	46	59	1.3
Ir2 [a]	252sh; 265; 284sh; 313sh; 381sh	502; 535; 575sh	4.9	15.0	683	2190	3.2

Table 1. *Cont.*

	λ_{abs} (nm)	λ_{em} (nm)	Φ_{aer} (%)	Φ_{deg} (%)	τ_{aer} (ns)	τ_{deaer} * (ns)	τ_{deg}/τ_{aer}
Ir3 [a]	255; 271sh; 291sh; 315sh; 348; 388sh; 424sh; 483sh	543sh; 573	4.0	14.1	1220	4210	3.5
Ir1 [b]		651			44	57	1.3
Ir2 [b]		503; 537; 577sh			700	2195	3.1
Ir3 [b]		542sh; 575			1240	4220	3.4
Ir1 [c]		650			61	66	1.1
Ir2 [c]		500; 532; 575sh			880	2210	2.5
Ir3 [c]		540sh; 575			1560	4215	2.7

[a] measured in water; [b] measured in 0.01M phosphate buffer saline solution; [c] measured in DMEM solution with 10% fetal bovine serum; excitation at 365 nm for emission and quantum yield measurements, 355 nm for excitation state lifetime measurements; * deaeration was not complete, residual O_2 concentration is shown in Table S1.

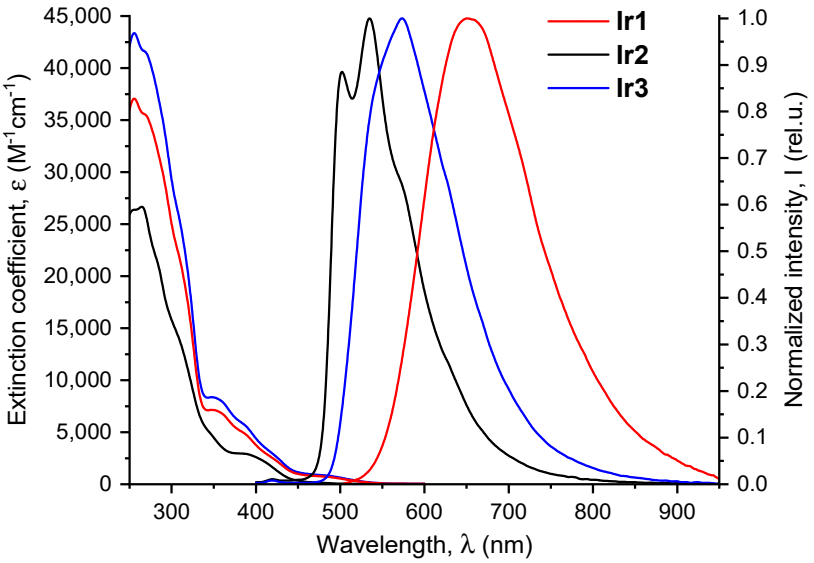

Figure 2. Absorption and emission spectra for complexes **Ir1**–**Ir3** in water (310 K, λ_{ex} 365 nm).

The DFT and TD DFT calculations (see Figure 3, Figures S19–S21, and Tables S2–S8) indicate that the lowest energy transitions in the absorption spectra of **Ir1**–**Ir3** are quite similar and may be described in terms of the mixed metal to ligand (^{1}MLCT) and ligand to ligand (^{1}LLCT, N^C→N^N#, N^C→N^C′) charge transfer with some contribution of the N^C ligand-centered (^{3}LC) transitions. However, emissive $T_1 \rightarrow S_0$ transitions display an essentially different nature, showing a mixture of ^{3}MLCT and ^{3}LLCT characters for **Ir1** (with N^N1 ligand as donor in the latter case), whereas emission of **Ir2** and **Ir3** occurs from the triplet excited state with the major contribution of the N^C ligand-centered (^{3}LC) character together with ^{3}MLCT (localized at N^C ligands). The location of the emissive triplet state mainly at the N^C ligand in **Ir2** and **Ir3** and the minimal contribution of the N^N ligand orbitals are evidently dictated by the lower energy of the N^N1 π* orbitals compared to those of N^N2 and N^N3 because of the electron-withdrawn substituents in N^N1. These observations are most probably responsible for the considerable difference (**Ir1** vs. **Ir2** and **Ir3**) in quantum yields and lifetimes for this group of compounds (see Table 1). It is also worth mentioning that the location of the emissive triplet at the cyclometallating N^C ligands in **Ir2** and **Ir3** results in higher availability of the chromophores for energy

transfer to oxygen molecules, thus giving the complexes a higher sensitivity to variations in O_2 concentration.

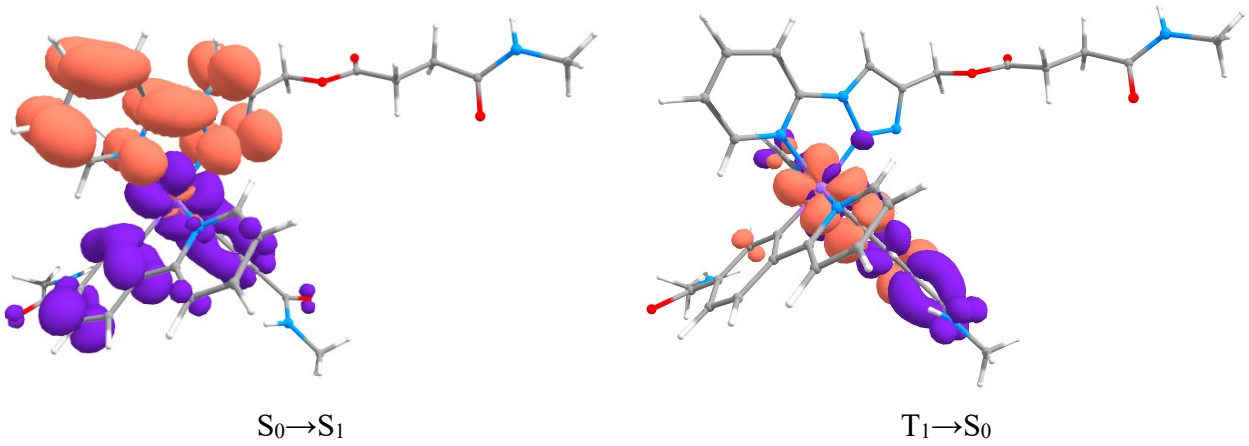

Figure 3. Natural transition orbitals (NTO) for **Ir2-0**, violet, and terracotta colors show decreases and increases in electron density, respectively. The calculations have been simplified by substituting OEG pendants of **Ir2** complex with methyl groups in **Ir2-0** structure. Atom colors: Ir-lilac; N-blue; O-red; C-gray, H-white.

For oxygen sensing experiments and bioimaging studies, we chose **Ir2** and **Ir3** complexes because these probes demonstrate high emission quantum yield (15.0% and 14.1%) and a much greater difference in the phosphorescence lifetime values in the aerated and deaerated water (3.2 and 3.5 times, respectively), see Table 1, compared with the **Ir1** probe (only 1.3 times), thus showing a stronger sensory response to O_2 molecules. To calibrate these promising oxygen probes, we studied the dependence of their lifetimes on the O_2 concentration (Figure 4 and Table S1) in different media, one of which (growth media DMEM with 10% fetal bovine serum—FBS) proved to be a very good model of the intracellular probe environment [44,45,47]. The standard Stern–Volmer calibrations gave linear $1/\tau$ vs. (O_2) dependences for both complexes in water, phosphate buffer saline (PBS), and DMEM-FBS solutions. It turned out that in aerated solutions in the presence of fetal bovine serum, these complexes display bi-exponential phosphorescence decay. However, the contribution of the second, longer exponent is insignificant (approximately 3–7%), so the data processing was carried out using a mono-exponential fit.

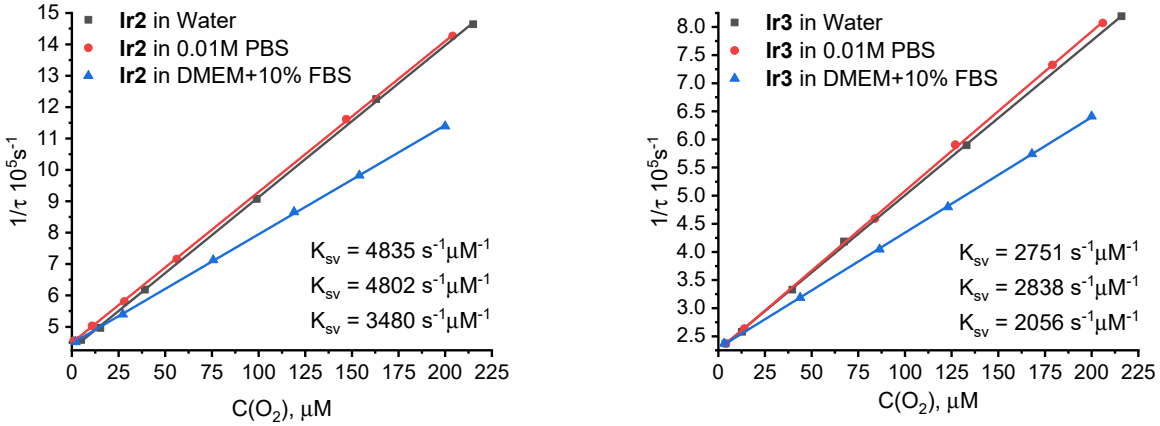

Figure 4. Stern–Volmer oxygen quenching plots of **Ir2** (**left**) and **Ir3** (**right**) in aqueous solution, 0.01 M PBS (pH 7.4), and in DMEM with 10% FBS. T = 37 °C, excitation at 355 nm.

The obtained data indicate that the oxygen sensitivity of **Ir2** and **Ir3** decreases in the presence of FBS, which results in a slightly different slope of the calibration plots and lower

values of Stern–Volmer constants (Figure 4). This deviation between the probe behavior in different media can be explained by an increase in the viscosity of the DMEM-FBS solution that affords a decrease in the oxygen diffusion coefficient, which also affects the collisional quenching of phosphorescence with oxygen. Despite the different slopes of the plots in water, PBS, and DMEM-FBS, all these calibrations gave the same lifetime values in deaerated solutions, which points to the preservation of the chromophores structure and their properties in all studied media. These observations indicate that **Ir2** and **Ir3** are promising for application as oxygen probes in PLIM experiments with live cells with the use of calibrations obtained in model physiological media.

3.3. Biological Experiments

Biological studies have shown that **Ir2** and **Ir3** complexes have low toxicity in mouse colorectal cancer cells CT26 (cell survival is about 90% up to concentrations of 125–150 μM, Figure 5). On the contrary, **Ir1** turned out to be more toxic, which, together with the more promising photophysical properties of **Ir2** and **Ir3**, predetermined the application of the latter compounds in the further bioimaging experiments. The low toxicity of these complexes, as well as their water solubility, is evidently explained by the introduction of hydrophilic biocompatible oligo(ethylene glycol) fragments in their structure.

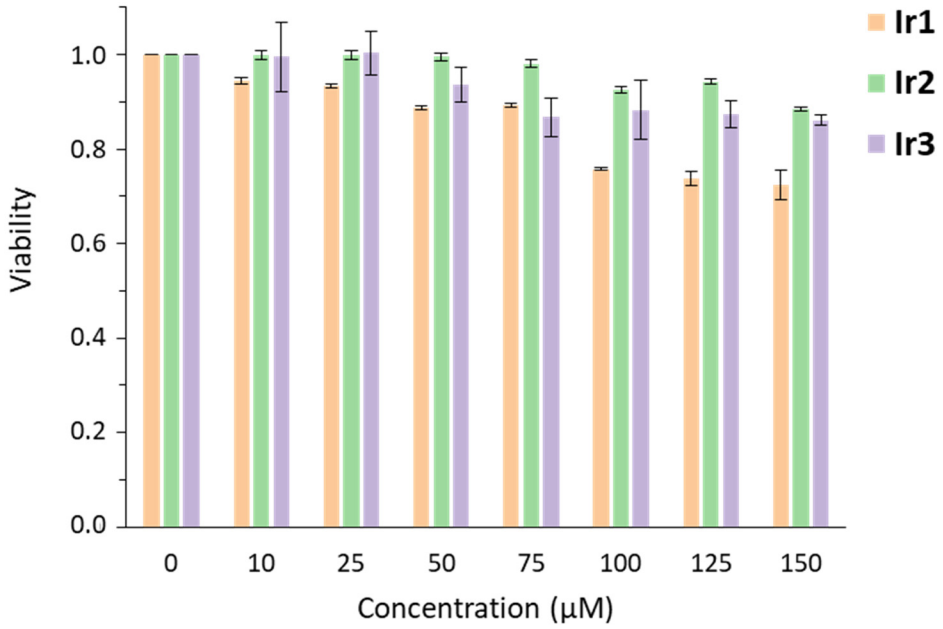

Figure 5. The MTT assay of CT26 cells after incubation with **Ir1**–**Ir3** in DMEM with 10% FBS. T = 37 °C, incubation for 24 h. The viability of control cells (without probe) was taken at 1. Black bars show the standard deviation. N = 3 repetitions.

Investigation of the internalization dynamics (Figure 6), carried out using confocal laser scanning microscopy, showed fast accumulation of the complexes **Ir2** and **Ir3** in cells in the initial period of time (up to 1 h), which then slows down. In the case of the **Ir3** complex, the intensity of its luminescence in cells practically reached maximum already after 5 h, whereas **Ir2** gave an appreciable luminescence intensity only after a day (see Figure 6 top). In addition, the **Ir3** complex displays more intense luminescence in cells compared to **Ir2**, which is probably due to both the faster dynamics of its accumulation and the stronger two-photon absorption at the excitation wavelength (750 nm).

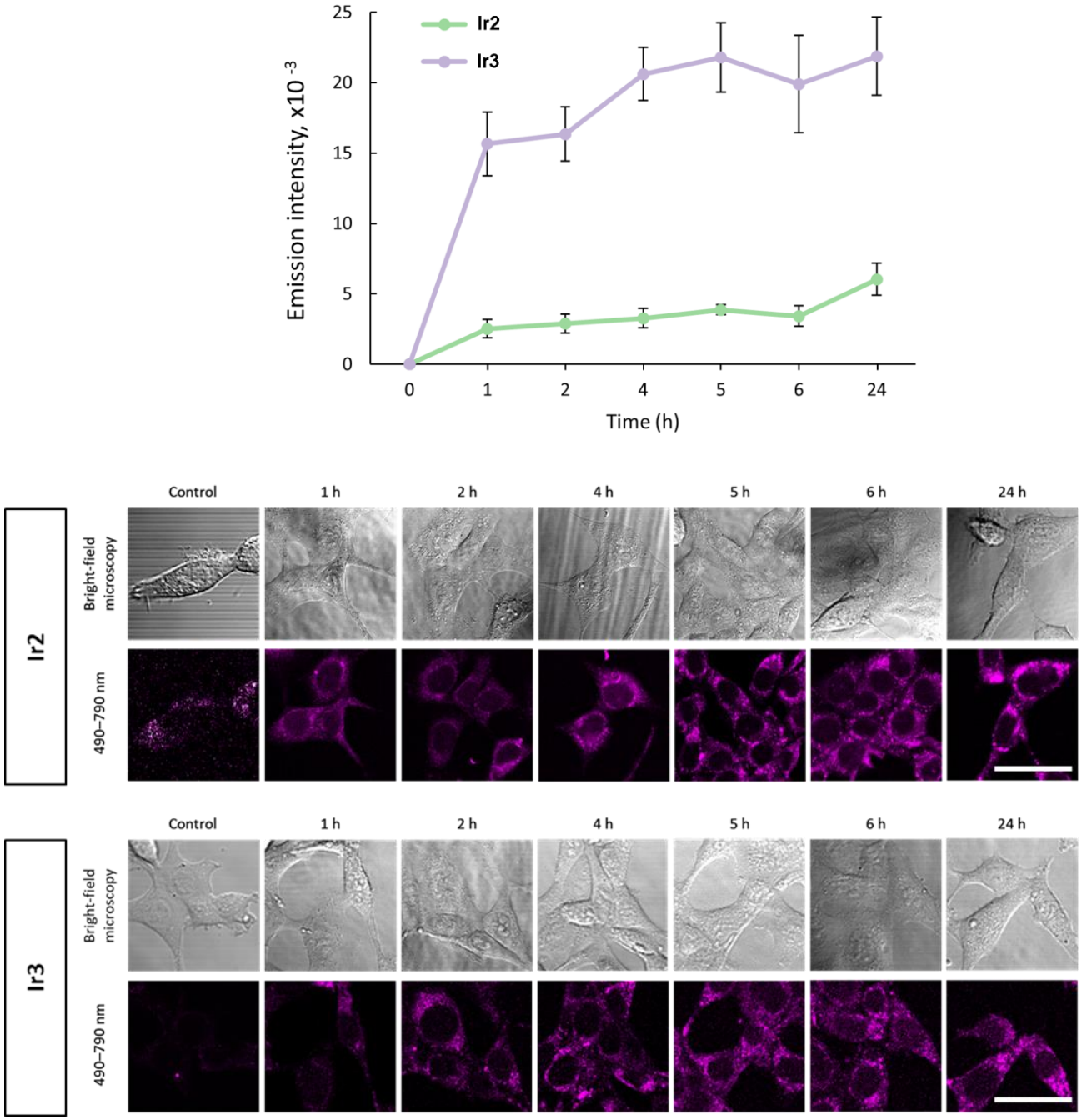

Figure 6. (**Top**): quantification of the internalization dynamics experiments of complexes **Ir2** and **Ir3** in CT26 cells after incubation with DMEM with 10% FBS. T = 37 °C, concentration of complexes, 25 μM. Emission intensity is shown as the mean ± standard deviation. (**Bottom**): representative microscopy images of cells in transmission channel and in luminescence channel (upper row, excitation 405 nm, recording 490–790 nm, purple color). Scale bar: 20 μm.

Both studied complexes showed a non-uniform distribution in cells but were accumulated in certain areas (Figure 7). Based on the colocalization data obtained for the **Ir2** complex with fluorescent trackers, it can be concluded that this probe was located in both lysosomes and mitochondria, while the **Ir3** compound was internalized primarily into mitochondria. The difference in internalization behavior of **Ir2** and **Ir3** can be most probably ascribed to a rather large hydrophobic fragment located at the N^N3 ligand. This makes the complex prone to preferential adsorption on the cell membrane, followed by its

transfer to mitochondria, because of its positive charge and negative mitochondrial potential. **Ir2** is essentially more hydrophilic and does not display selectivity in internalization using both membrane sorption and endocytosis. Therefore, the **Ir3** probe can be used in the experiments aimed at simultaneous monitoring of the response of cells to changes in oxygen concentration (by the phosphorescence lifetime of the complex) and determination of cell metabolic status (by the fluorescence lifetime of the metabolic cofactor—reduced nicotinamide adenine dinucleotide (phosphate)—NAD(P)H) [43].

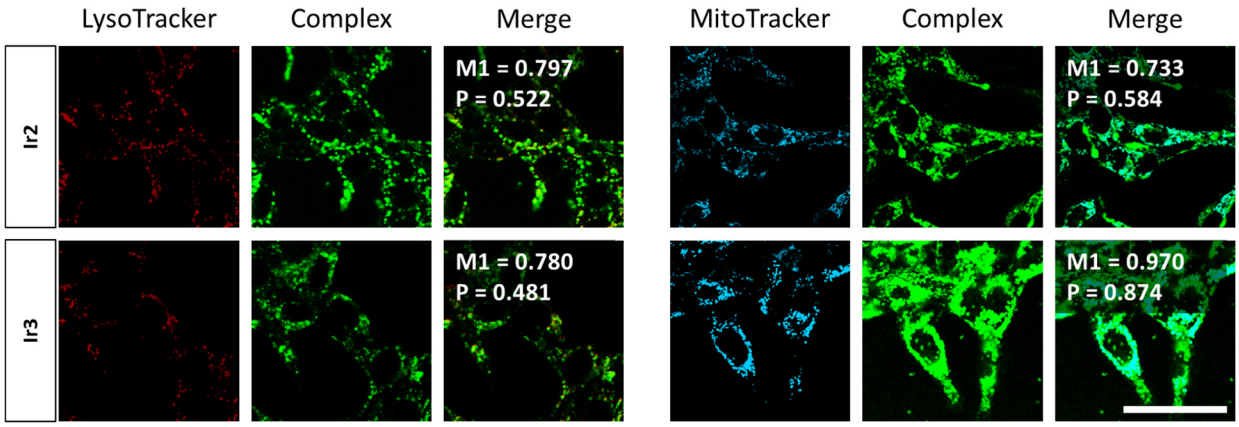

Figure 7. Subcellular distribution of **Ir2** (**top row**) and **Ir3** (**bottom row**) in CT26 cells (green color). Co-staining of cells with the complexes and organelle-specific dyes for mitochondria (BioTracker 405 Blue Mitochondria Dye) and lysosomes (LysoTracker Red DND-99). Pearson's (P) and Manders' overlap coefficients (M1, the tracker signal overlaps the complex) are presented on merge images. Scale bar: 50 μm.

We also carried out PLIM experiments with **Ir2** and **Ir3** complexes on the CT26 cells under normal conditions and simulated hypoxia (Figure 8). The phosphorescence lifetime of the **Ir2** complex, measured inside the cells by the PLIM method, ranged from 900 to 1300 ns under normoxic conditions to 1500–1800 ns under hypoxia. The phosphorescence lifetime increased similarly for **Ir3** from 1900–2300 ns to 3100–3300 ns. It should be noted that the indicated lifetime values are very close to those obtained in a cuvette for a model biological medium (DMEM, with the addition of 10% FBS) and clearly reflect the oxygen concentration variations between normoxic and hypoxic conditions in the cells.

However, for both cases, there was a slight increase in the lifetime of cells under normoxia compared with the calibration data on solutions. This is probably due to the consumption of oxygen by the cells and, as a result, a somewhat lower O_2 content compared to the solution saturated with air. A lower oxygen content in the incubation atmosphere (19.5% instead of 21% in air) also has to be taken into account, as does a slower oxygen diffusion in cells due to the presence of a number of different structures and biomacromolecules and a higher media viscosity. The effects of these media characteristics are very similar for **Ir2** and **Ir3** probes and can be easily seen in the lifetime variations between normoxia and hypoxia, which are of the order of 3.2–3.5 in aqueous solutions, 2.5–2.7 in the growth medium, and only about 1.5 in cells.

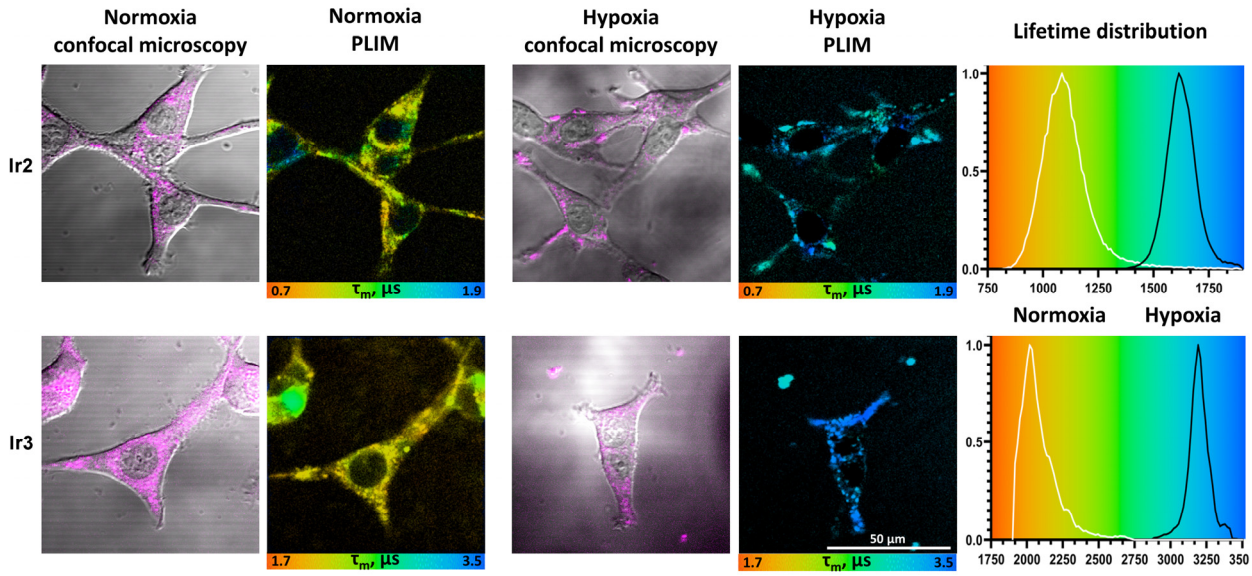

Figure 8. Confocal microscopic images and PLIM images of CT26 cells incubated with complexes **Ir2** (**top**) and **Ir3** (**bottom**) (100 μM, 24 h) under normoxia and hypoxia conditions. Hypoxia was induced by covering the cell monolayer with a coverglass for 1 h. Confocal images are presented as merged luminescence images and DIC (differential interference contrast). In PLIM, colors correspond to the lifetime in the range of 700–1900 ns for **Ir2** and 1700–3500 ns for **Ir3**. Lifetime distributions are calculated for the whole PLIM image. Two photon excitations at 750 nm, T = 37 °C, and 5% CO_2.

4. Conclusions

Three new luminescent bis-cyclometallated iridium $[Ir(N^{\wedge}C)_2(N^{\wedge}N)]^+$ complexes with various di-imine ligands were obtained and characterized. To impart them water solubility and biocompatibility, the compounds were decorated with short-branched oligo(ethylene glycol) fragments attached both to the N^C and N^N ligands. The photophysical study of these emitters in aqueous media showed that they exhibit phosphorescence, with quantum yields up to 15% in a deaerated aqueous solution.

The applied di-imine ligands noticeably differ from each other in the nature of their electronic and structural characteristics, as well as in their hydrophobic–hydrophilic properties. Indeed, it turned out that the resulting complexes exhibit significantly different photophysical properties that are due to the different influence and contribution of di-imine ligands to the excitation processes and emissive relaxation. We also found significant variations in the biological properties of the obtained probes (toxicity, localization, and internalization), which are evidently due to differences in the nature of the ligands (N^N3 is the most hydrophobic of the ligands used, N^N2 is significantly more hydrophilic, and N^N1 contains twice as many OEG-groups as its counterparts N^N2 and N^N3).

According to the results of DFT and TD DFT calculations, the nature of the transitions responsible for emission of the two most efficient phosphors (**Ir2** and **Ir3** complexes) is associated with the formation of the N^C ligand-centered excited state that gave appreciable lifetime sensitivity to the variations in molecular oxygen concentration in various aqueous media, ca. 3.3 times increase upon deaeration of water and PBS and ca. 2.6 in model physiological solution (DMEM with 10% FBS).

The investigations of the obtained compounds in bioimaging experiments confirmed their applicability as effective and low-toxic O_2 molecular probes. The **Ir3** complex is primarily localized in cell mitochondria, whereas **Ir2** displays localization in mitochondria and lysosomes. PLIM studies of the CT26 cells incubated with these probes showed a significant change in the phosphorescence lifetime values during the transition from normoxia to simulated hypoxia. Moreover, the lifetime values obtained for complexes inside cells are very close to the values measured in a cuvette in a model biological medium,

which indicates an opportunity to apply these probes for semi-quantitative estimation of oxygen concentration in biological samples with the PLIM technique and pave the way for the use of these probes in in vivo experiments.

Supplementary Materials: The following supporting information can be downloaded at: https://www.mdpi.com/article/10.3390/chemosensors11050263/s1, File S1: optimized structures of complexes **Ir1-0**, **Ir2-0**, **Ir3-0**. References [54–63] are cited in the supplementary materials. Figure S1. ^{1}H NMR spectrum of N^C, $CDCl_3$, 298 K. Figure S2. ^{1}H-^{1}H COSY NMR spectra of N^C, $CDCl_3$, 298 K. Figure S3. ESI$^+$ mass-spectrum of N^C ([M + H]+cation area), solvent–methanol. Figure S4. ^{1}H NMR spectrum of N^N1, $(CD_3)_2CO$, 298 K. Figure S5. ^{1}H-^{1}H COSY NMR spectra of N^N1, $(CD_3)_2CO$, 298 K. Figure S6. ESI$^+$ mass-spectrum of N^N1 ([M + H]+cation area), solvent–methanol. Figure S7. ^{1}H NMR spectrum of dissociated dimer $[Ir_2(N^C)_4Cl_2]$, $(CD_3)_2SO$, 298 K. Figure S8. ^{1}H-^{1}H COSY NMR spectra of dissociated dimer $[Ir_2(N^C)_4Cl_2]$, $(CD_3)_2SO$, 298 K. Figure S9. ESI$^+$ mass-spectrum of dimer $[Ir_2(N^C)_4Cl_2]$ ($[Ir(N^C)_2]$+cation area), solvent–methanol. Figure S10. ^{1}H NMR spectrum of **Ir1**, CD_3OD, 298 K. Figure S11. ^{1}H-^{1}H COSY NMR spectra of **Ir1**, CD_3OD, 298 K. Figure S12. ESI$^+$ mass-spectrum of **Ir1** ($[M + Na]^{2+}$cation area), solvent–methanol. Figure S13. ^{1}H NMR spectrum of **Ir2**, CD_3OD, 298 K. Figure S14. ^{1}H-^{1}H COSY NMR spectra of **Ir2**, CD_3OD, 298 K. Figure S15. ESI$^+$ mass-spectrum of **Ir2** ($[M + Na]^{2+}$cation area), solvent–methanol. Figure S16. ^{1}H NMR spectrum of **Ir3**, CD_3OD, 298 K. Figure S17. ^{1}H-^{1}H COSY NMR spectra of **Ir3**, CD_3OD, 298 K. Figure S18. ESI$^+$ mass-spectrum of **Ir3** ($[M + Na]^{2+}$cation area), solvent–methanol. Figure S19. Absorption spectra of **Ir1**: experimental (red) and calculated (black) lines with oscillator strengths of electronic transitions (bars). Figure S20. Absorption spectra of **Ir2**: experimental (red) and calculated (black) lines with oscillator strengths of electronic transitions (bars). Figure S21. Absorption spectra of **Ir3**: experimental (red) and calculated (black) lines with oscillator strengths of electronic transitions (bars). Figure S22. Optimized structure of the model **Ir2-0** complex (hydrogen atoms are omitted for clarity). The calculations have been simplified by substitution of OEG pendants in **Ir2** complex with methyl groups in **Ir2-0** structure. Figure S23. Optimized structure of the model **Ir3-0** complex (hydrogen atoms are omitted for clarity). The calculations have been simplified by substitution of OEG pendants in **Ir3** complex with methyl groups in **Ir3-0** structure. Table S1. Values of excitation state lifetime of complexes **Ir2** and **Ir3** in various aqueous media and at different oxygen concentrations. Table S2. Calculated and experimental wavelength of emission maxima of complexes **Ir1**–**Ir3**. Table S3. Calculated absorption maxima (λ) and oscillator strengths (f) of complex **Ir1**. Table S4. The decrease (violet) and increase (terracotta) of electron density for most intensive electronic absorption transitions of **Ir1**. Table S5. Calculated absorption maxima (λ) and oscillator strengths (f) of complex **Ir2**. Table S6. The decrease (violet) and increase (terracotta) of electron density for most intensive electronic absorption transitions of **Ir2**. Table S7. Calculated absorption maxima (λ) and oscillator strengths (f) of complex **Ir3**. Table S8. The decrease (violet) and increase (terracotta) of electron density for most intensive electronic absorption transitions of **Ir3**. Table S9. The key structural parameters of complex **Ir1-0**, **Ir2-0**, **Ir3-0** (R = Me) and its literature analog.

Author Contributions: Conceptualization, S.P.T. and I.S.K.; methodology, I.S.K. and M.V.S.; validation, M.V.S.; investigation, M.S., D.O.K. and A.D.K.; data curation, I.S.K.; writing—original draft preparation, I.S.K., M.S., D.O.K. and A.D.K.; writing—review and editing, S.P.T. and M.V.S.; supervision, S.P.T.; project administration, I.S.K.; funding acquisition, I.S.K. All authors have read and agreed to the published version of the manuscript.

Funding: This research was funded by the Russian Science Foundation, grant number 18-73-10021.

Institutional Review Board Statement: Biological studies were approved be the Local Ethics Committee of the Privolzhsky Research Medical University (protocol № 15 from 23 September 2022).

Informed Consent Statement: Not applicable.

Data Availability Statement: No data are available.

Acknowledgments: In commemoration of the 300th anniversary of St. Petersburg State University's founding. This work was performed using the equipment of the Centers for Magnetic Resonance, for Optical and Laser Materials Research, for Chemical Analysis and Materials Research, the Computer Center, and the Cryogenic Center of the Research Park of St. Petersburg State University.

Conflicts of Interest: The authors declare no conflict of interest.

References

1. Semenza, G.L. Life with Oxygen. *Science* **2007**, *318*, 62–64. [CrossRef] [PubMed]
2. Semenza, G.L. Hypoxia-Inducible Factors in Physiology and Medicine. *Cell* **2012**, *148*, 399–408. [CrossRef] [PubMed]
3. Clanton, T.L.; Hogan, M.C.; Gladden, L.B. Regulation of Cellular Gas Exchange, Oxygen Sensing, and Metabolic Control. *Compr. Physiol.* **2013**, *3*, 1135–1190. [CrossRef]
4. Tsai, A.G.; Johnson, P.C.; Intaglietta, M. Oxygen Gradients in the Microcirculation. *Physiol. Rev.* **2003**, *83*, 933–963. [CrossRef]
5. Borisov, S.M. CHAPTER 1 Fundamentals of Quenched Phosphorescence O_2 Sensing and Rational Design of Sensor Materials. In *Quenched-Phosphorescence Detection of Molecular Oxygen: Applications in Life Sciences*; The Royal Society of Chemistry: London, UK, 2018; pp. 1–18, ISBN 978-1-78801-175-4.
6. Mycek, M.A.; Pogue, B.W. *Handbook of Biomedical Fluorescence*; CRC Press: Boca Raton, FL, USA, 2003; ISBN 9781135542580.
7. Jenkins, J.; Dmitriev, R.I.; Papkovsky, D.B. Imaging Cell and Tissue O_2 by TCSPC-PLIM. In *Advanced Time-Correlated Single Photon Counting Applications*; Becker, W., Ed.; Springer International Publishing: Cham, Switzerland, 2015; pp. 225–247, ISBN 978-3-319-14929-5.
8. Papkovsky, D.B.; Dmitriev, R.I. Imaging of oxygen and hypoxia in cell and tissue samples. *Cell. Mol. Life Sci.* **2018**, *75*, 2963–2980. [CrossRef] [PubMed]
9. Papkovsky, D.B.; Zhdanov, A.V. Phosphorescence based oxygen sensors and probes for biomedical research. In *Advanced Environmental, Chemical, and Biological Sensing Technologies XIV*; SPIE: Bellingham, WA, USA, 2017; Volume 10215, pp. 102–108. [CrossRef]
10. Chelushkin, P.S.; Shakirova, J.R.; Kritchenkov, I.S.; Baigildin, V.A.; Tunik, S.P. Phosphorescent NIR emitters for biomedicine: Applications, advances and challenges. *Dalton Trans.* **2021**, *51*, 1257–1280. [CrossRef]
11. Cheng, M.H.Y.; Mo, Y.; Zheng, G. Nano versus Molecular: Optical Imaging Approaches to Detect and Monitor Tumor Hypoxia. *Adv. Health Mater.* **2020**, *10*, e2001549. [CrossRef]
12. Dmitriev, R.I.; Papkovsky, D.B. Intracellular probes for imaging oxygen concentration: How good are they? *Methods Appl. Fluoresc.* **2015**, *3*, 034001. [CrossRef]
13. Carraway, E.R.; Demas, J.N.; DeGraff, B.A.; Bacon, J.R. Photophysics and photochemistry of oxygen sensors based on luminescent transition-metal complexes. *Anal. Chem.* **1991**, *63*, 337–342. [CrossRef]
14. Baggaley, E.; Weinstein, J.A.; Williams, J.A.G. Time-Resolved Emission Imaging Microscopy Using Phosphorescent Metal Complexes: Taking FLIM and PLIM to New Lengths. *Struct. Bond.* **2014**, *165*, 205–256. [CrossRef]
15. Yoshihara, T.; Hirakawa, Y.; Hosaka, M.; Nangaku, M.; Tobita, S. Oxygen imaging of living cells and tissues using luminescent molecular probes. *J. Photochem. Photobiol. C Photochem. Rev.* **2017**, *30*, 71–95. [CrossRef]
16. Tsytsarev, V.; Papkovsky, D.B. CHAPTER 16 In vivo Brain Functional Imaging Using Oxygenation-related Optical Signal. In *Quenched-Phosphorescence Detection of Molecular Oxygen: Applications in Life Sciences*; The Royal Society of Chemistry: London, UK, 2018; pp. 319–334, ISBN 978-1-78801-175-4.
17. Pogue, B.W.; Zhang, R.; Cao, X.; Jia, J.M.; Petusseau, A.; Bruza, P.; Vinogradov, S.A. Review of in vivo optical molecular imaging and sensing from X-ray excitation. *J. Biomed. Opt.* **2021**, *26*, 010902. [CrossRef] [PubMed]
18. Dmitriev, R.I.; Borisov, S.M.; Kondrashina, A.V.; Pakan, J.M.P.; Anilkumar, U.; Prehn, J.H.M.; Zhdanov, A.V.; McDermott, K.W.; Klimant, I.; Papkovsky, D.B. Imaging oxygen in neural cell and tissue models by means of anionic cell-permeable phosphorescent nanoparticles. *Cell. Mol. Life Sci.* **2014**, *72*, 367–381. [CrossRef]
19. Zhdanov, A.V.; Okkelman, I.A.; Golubeva, A.V.; Doerr, B.; Hyland, N.P.; Melgar, S.; Shanahan, F.; Cryan, J.F.; Papkovsky, D.B. Quantitative analysis of mucosal oxygenation using ex vivo imaging of healthy and inflamed mammalian colon tissue. *Cell. Mol. Life Sci.* **2016**, *74*, 141–151. [CrossRef] [PubMed]
20. Dmitriev, R.I.; Zhdanov, A.V.; Nolan, Y.M.; Papkovsky, D.B. Imaging of neurosphere oxygenation with phosphorescent probes. *Biomaterials* **2013**, *34*, 9307–9317. [CrossRef]
21. Kondrashina, A.V.; Dmitriev, R.I.; Borisov, S.M.; Klimant, I.; O'Brien, I.; Nolan, Y.M.; Zhdanov, A.V.; Papkovsky, D.B. A Phosphorescent Nanoparticle-Based Probe for Sensing and Imaging of (Intra)Cellular Oxygen in Multiple Detection Modalities. *Adv. Funct. Mater.* **2012**, *22*, 4931–4939. [CrossRef]
22. Tsytsarev, V.; Arakawa, H.; Borisov, S.; Pumbo, E.; Erzurumlu, R.S.; Papkovsky, D.B. In vivo imaging of brain metabolism activity using a phosphorescent oxygen-sensitive probe. *J. Neurosci. Methods* **2013**, *216*, 146–151. [CrossRef]
23. Dmitriev, R.I.; Borisov, S.M.; Düssmann, H.; Sun, S.; Müller, B.J.; Prehn, J.; Baklaushev, V.P.; Klimant, I.; Papkovsky, D.B. Versatile Conjugated Polymer Nanoparticles for High-Resolution O_2 Imaging in Cells and 3D Tissue Models. *ACS Nano* **2015**, *9*, 5275–5288. [CrossRef]
24. Papkovsky, D.B.; Dmitriev, R.I.; Borisov, S. Imaging of oxygenation in 3D tissue models with multi-modal phosphorescent probes. In *Multiphoton Microscopy in the Biomedical Sciences XV*; SPIE: Bellingham, WA, USA, 2015; Volume 9329, pp. 33–38.
25. Dmitriev, R.I.; Papkovsky, D.B. Multi-parametric O_2 Imaging in Three-Dimensional Neural Cell Models with the Phosphorescent Probes. *Methods Mol. Biol.* **2014**, *1254*, 55–71. [CrossRef]
26. Fercher, A.; Borisov, S.M.; Zhdanov, A.V.; Klimant, I.; Papkovsky, D.B. Intracellular O_2 Sensing Probe Based on Cell-Penetrating Phosphorescent Nanoparticles. *ACS Nano* **2011**, *5*, 5499–5508. [CrossRef]
27. Okkelman, I.A.; Foley, T.; Papkovsky, D.B.; Dmitriev, R.I. Live cell imaging of mouse intestinal organoids reveals heterogeneity in their oxygenation. *Biomaterials* **2017**, *146*, 86–96. [CrossRef] [PubMed]

28. Zhdanov, A.V.; Golubeva, A.V.; Okkelman, I.A.; Cryan, J.F.; Papkovsky, D.B. Imaging of oxygen gradients in giant umbrella cells: An ex vivo PLIM study. *Am. J. Physiol. Physiol.* **2015**, *309*, C501–C509. [CrossRef] [PubMed]
29. Dmitriev, R.I.; Borisov, S.M.; Jenkins, J.; Papkovsky, D.B. Multi-parametric imaging of tumor spheroids with ultra-bright and tunable nanoparticle O_2 probes. In *Imaging, Manipulation, and Analysis of Biomolecules, Cells, and Tissues XIII*; SPIE: Bellingham, WA, USA, 2015; Volume 9328, pp. 12–19. [CrossRef]
30. Şencan, I.; Esipova, T.V.; Yaseen, M.A.; Fu, B.; Boas, D.A.; Vinogradov, S.A.; Shahidi, M.; Sakadžić, S. Two-photon phosphorescence lifetime microscopy of retinal capillary plexus oxygenation in mice. *J. Biomed. Opt.* **2018**, *23*, 126501. [CrossRef]
31. Christodoulou, C.; Spencer, J.A.; Yeh, S.-C.A.; Turcotte, R.; Kokkaliaris, K.D.; Panero, R.; Ramos, A.; Guo, G.; Seyedhassantehrani, N.; Esipova, T.V.; et al. Live-animal imaging of native haematopoietic stem and progenitor cells. *Nature* **2020**, *578*, 278–283. [CrossRef]
32. Cao, X.; Allu, S.R.; Jiang, S.; Jia, M.; Gunn, J.R.; Yao, C.; LaRochelle, E.P.; Shell, J.R.; Bruza, P.; Gladstone, D.J.; et al. Tissue pO_2 distributions in xenograft tumors dynamically imaged by Cherenkov-excited phosphorescence during fractionated radiation therapy. *Nat. Commun.* **2020**, *11*, 573. [CrossRef] [PubMed]
33. Pogue, B.W.; Feng, J.; LaRochelle, E.P.; Bruža, P.; Lin, H.; Zhang, R.; Shell, J.R.; Dehghani, H.; Davis, S.C.; Vinogradov, S.A.; et al. Maps of in vivo oxygen pressure with submillimetre resolution and nanomolar sensitivity enabled by Cherenkov-excited luminescence scanned imaging. *Nat. Biomed. Eng.* **2018**, *2*, 254–264. [CrossRef] [PubMed]
34. Roussakis, E.; Spencer, J.A.; Lin, C.P.; Vinogradov, S.A. Two-Photon Antenna-Core Oxygen Probe with Enhanced Performance. *Anal. Chem.* **2014**, *86*, 5937–5945. [CrossRef]
35. Şencan, I.; Esipova, T.; Kılıç, K.; Li, B.; Desjardins, M.; Yaseen, M.A.; Wang, H.; Porter, J.E.; Kura, S.; Fu, B.; et al. Optical measurement of microvascular oxygenation and blood flow responses in awake mouse cortex during functional activation. *J. Cereb. Blood Flow Metab.* **2020**, *42*, 510–525. [CrossRef]
36. Spencer, J.A.; Ferraro, F.; Roussakis, E.; Klein, A.; Wu, J.; Runnels, J.M.; Zaher, W.; Mortensen, L.J.; Alt, C.; Turcotte, R.; et al. Direct measurement of local oxygen concentration in the bone marrow of live animals. *Nature* **2014**, *508*, 269–273. [CrossRef]
37. Sakadžić, S.; Roussakis, E.; Yaseen, M.A.; Mandeville, E.T.; Srinivasan, V.J.; Arai, K.; Ruvinskaya, S.; Devor, A.; Lo, E.H.; Vinogradov, S.A.; et al. Two-photon high-resolution measurement of partial pressure of oxygen in cerebral vasculature and tissue. *Nat. Methods* **2010**, *7*, 755–759. [CrossRef]
38. Rytelewski, M.; Haryutyunan, K.; Nwajei, F.; Shanmugasundaram, M.; Wspanialy, P.; Zal, M.A.; Chen, C.-H.; El Khatib, M.; Plunkett, S.; Vinogradov, S.A.; et al. Merger of dynamic two-photon and phosphorescence lifetime microscopy reveals dependence of lymphocyte motility on oxygen in solid and hematological tumors. *J. Immunother. Cancer* **2019**, *7*, 78. [CrossRef] [PubMed]
39. Esipova, T.V.; Karagodov, A.; Miller, J.; Wilson, D.F.; Busch, T.M.; Vinogradov, S.A. Two New "Protected" Oxyphors for Biological Oximetry: Properties and Application in Tumor Imaging. *Anal. Chem.* **2011**, *83*, 8756–8765. [CrossRef] [PubMed]
40. Esipova, T.V.; Barrett, M.J.; Erlebach, E.; Masunov, A.E.; Weber, B.; Vinogradov, S.A. Oxyphor 2P: A High-Performance Probe for Deep-Tissue Longitudinal Oxygen Imaging. *Cell Metab.* **2019**, *29*, 736–744.e7. [CrossRef] [PubMed]
41. Dmitriev, R.I.; Kondrashina, A.V.; Koren, K.; Klimant, I.; Zhdanov, A.V.; Pakan, J.M.P.; McDermott, K.W.; Papkovsky, D.B. Small molecule phosphorescent probes for O_2 imaging in 3D tissue models. *Biomater. Sci.* **2014**, *2*, 853–866. [CrossRef]
42. Shirmanova, M.V.; Shcheslavskiy, V.I.; Lukina, M.M.; Dudenkova, V.V.; Kritchenkov, I.; Solomatina, A.; Tunik, S.P. Molecular oxygen mapping in biological samples by time-correlated single photon counting technique and Ir(III)-based complexes. In *Optical Biopsy XVIII: Toward Real-Time Spectroscopic Imaging and Diagnosis*; SPIE: Bellingham, WA, USA, 2020; Volume 11234, pp. 26–33. [CrossRef]
43. Rueck, A.C.; Schäfer, P.; von Einem, B.; Kalinina, S. Metabolic NADH/FAD/FMN FLIM and oxygen PLIM: Multiphoton luminescence lifetime imaging on the way to clinical diagnosis. In *Multiphoton Microscopy in the Biomedical Sciences XX*; SPIE: Bellingham, WA, USA, 2020; Volume 11244, pp. 6–13. [CrossRef]
44. Kritchenkov, I.S.; Elistratova, A.A.; Sokolov, V.V.; Chelushkin, P.S.; Shirmanova, M.V.; Lukina, M.M.; Dudenkova, V.V.; Shcheslavskiy, V.I.; Kalinina, S.; Reeß, K.; et al. A biocompatible phosphorescent Ir(iii) oxygen sensor functionalized with oligo(ethylene glycol) groups: Synthesis, photophysics and application in PLIM experiments. *New J. Chem.* **2020**, *44*, 10459–10471. [CrossRef]
45. Kritchenkov, I.S.; Solomatina, A.I.; Kozina, D.O.; Porsev, V.V.; Sokolov, V.V.; Shirmanova, M.V.; Lukina, M.M.; Komarova, A.D.; Shcheslavskiy, V.I.; Belyaeva, T.N.; et al. Biocompatible Ir(III) Complexes as Oxygen Sensors for Phosphorescence Lifetime Imaging. *Molecules* **2021**, *26*, 2898. [CrossRef]
46. Kritchenkov, I.S.; Solomatina, A.I.; Chelushkin, P.S.; Shirmanova, M.V.; Kornilova, E.S.; Rueck, A.; Tunik, S.P. Phosphorescent Ir(III) oxygen sensors for bioimaging. In Proceedings of the 2022 International Conference Laser Optics (ICLO), St. Petersburg, Russia, 20–24 June 2022; p. 1.
47. Kritchenkov, I.S.; Mikhnevich, V.G.; Stashchak, V.S.; Solomatina, A.I.; Kozina, D.O.; Sokolov, V.V.; Tunik, S.P. Novel NIR-Phosphorescent Ir (III) Complexes: Synthesis, Characterization and Their Exploration as Lifetime-Based O_2 Sensors in Living Cells. *Molecules* **2022**, *27*, 3156. [CrossRef]
48. Elistratova, A.A.; Kritchenkov, I.S.; Lezov, A.A.; Gubarev, A.S.; Solomatina, A.I.; Kachkin, D.V.; Shcherbina, N.A.; Liao, Y.-C.; Liu, Y.-C.; Yang, Y.-Y.; et al. Lifetime oxygen sensors based on block copolymer micelles and non-covalent human serum albumin adducts bearing phosphorescent near-infrared iridium(III) complex. *Eur. Polym. J.* **2021**, *159*, 110761. [CrossRef]
49. Oki, A.R.; Morgan, R.J. An efficient preparation of 4, 4′-dicarboxy-2, 2′-bipyridine. *Synth. Commun.* **1995**, *25*, 4093–4097. [CrossRef]

50. McCarney, E.P.; Hawes, C.S.; Blasco, S.; Gunnlaugsson, T. Synthesis and structural studies of 1,4-di(2-pyridyl)-1,2,3-triazole dpt and its transition metal complexes; a versatile and subtly unsymmetric ligand. *Dalt. Trans.* **2016**, *45*, 10209–10221. [CrossRef]
51. Kritchenkov, I.S.; Chelushkin, P.S.; Sokolov, V.V.; Pavlovskiy, V.V.; Porsev, V.V.; Evarestov, R.A.; Tunik, S.P. Near-Infrared $[Ir(N^{\wedge}C)_2(N^{\wedge}N)]^+$ Emitters and Their Noncovalent Adducts with Human Serum Albumin: Synthesis and Photophysical and Computational Study. *Organometallics* **2019**, *38*, 3740–3751. [CrossRef]
52. Samudrala, R.; Zhang, X.; Wadkins, R.M.; Mattern, D.L. Synthesis of a non-cationic, water-soluble perylenetetracarboxylic diimide and its interactions with G-quadruplex-forming DNA. *Bioorganic Med. Chem.* **2007**, *15*, 186–193. [CrossRef] [PubMed]
53. Kritchenkov, I.S.; Zhukovsky, D.D.; Mohamed, A.; Korzhikov-Vlakh, V.A.; Tennikova, T.B.; Lavrentieva, A.; Scheper, T.; Pavlovskiy, V.V.; Porsev, V.V.; Evarestov, R.A.; et al. Functionalized Pt(II) and Ir(III) NIR Emitters and Their Covalent Conjugates with Polymer-Based Nanocarriers. *Bioconjugate Chem.* **2020**, *31*, 1327–1343. [CrossRef] [PubMed]
54. Hanss, D.; Freys, J.C.; Bernardinelli, G.; Wenger, O.S. Cyclometalated Iridium(III) Complexes as Photosensitizers for Long-Range Electron Transfer: Occurrence of a Coulomb Barrier. *Eur. J. Inorg. Chem.* **2009**, *2009*, 4850–4859. [CrossRef]
55. Su, N.; Lu, G.-Z.; Zheng, Y.-X. Highly efficient green electroluminescence of iridium(iii) complexes based on (1*H*-pyrazol-5-yl)pyridine derivatives ancillary ligands with low efficiency roll-off. *J. Mater. Chem. C* **2018**, *6*, 5778–5784. [CrossRef]
56. Solomatina, A.I.; Kuznetsov, K.M.; Gurzhiy, V.V.; Pavlovskiy, V.V.; Porsev, V.V.; Evarestov, R.A.; Tunik, S.P. Luminescent organic dyes containing a phenanthro[9,10-*D*]imidazole core and $[Ir(N^{\wedge}C)(N^{\wedge}N)]^+$ complexes based on the cyclometalating and diimine ligands of this type. *Dalton Trans.* **2020**, *49*, 6751–6763. [CrossRef]
57. Frisch, M.J.; Trucks, G.W.; Schlegel, H.B.; Scuseria, G.E.; Robb, M.A.; Cheeseman, J.R.; Scalmani, G.; Barone, V.; Petersson, G.A.; Nakatsuji, H.; et al. *Gaussian 16, Revision B.01*; Gaussian: Wallingford, CT, USA, 2016.
58. Austin, A.; Petersson, G.A.; Frisch, M.J.; Dobek, F.J.; Scalmani, G.; Throssell, K. A Density Functional with Spherical Atom Dispersion Terms. *J. Chem. Theory Comput.* **2012**, *8*, 4989–5007. [CrossRef]
59. Dolg, M.; Wedig, U.; Stoll, H.; Preuss, H. Energy-adjusted ab initio pseudopotentials for the first row transition elements. *J. Chem. Phys.* **1987**, *86*, 866–872. [CrossRef]
60. Tomasi, J.; Mennucci, B.; Cammi, R. Quantum Mechanical Continuum Solvation Models. *Chem. Rev.* **2005**, *105*, 2999–3094. [CrossRef]
61. O'boyle, N.M.; Tenderholt, A.L.; Langner, K.M. cclib: A library for package-independent computational chemistry algorithms. *J. Comput. Chem.* **2008**, *29*, 839–845. [CrossRef]
62. Martin, R.L. Natural transition orbitals. *J. Chem. Phys.* **2003**, *118*, 4775–4777. [CrossRef]
63. Lu, T.; Chen, F. Multiwfn: A multifunctional wavefunction analyzer. *J. Comput. Chem.* **2012**, *33*, 580–592. [CrossRef] [PubMed]